


Combined diffusion-relaxometry MRI to identify dysfunction in the human placenta

Paddy J. Slator^{1*}  | Jana Hutter^{2,3*} | Marco Palombo¹ | Laurence H. Jackson^{2,3} | Alison Ho⁴ | Eleftheria Panagiotaki¹ | Lucy C. Chappell⁴ | Mary A. Rutherford³ | Joseph V. Hajnal^{2,3} | Daniel C. Alexander¹

¹Centre for Medical Image Computing and Department of Computer Science, University College London, London, United Kingdom

²Biomedical Engineering Department, King's College London, London, United Kingdom

³Centre for the Developing Brain, King's College London, London, United Kingdom

⁴Women's Health Department, King's College London, London, United Kingdom

Correspondence

Paddy J. Slator PhD, Centre for Medical Image Computing, Department of Computer Science, University College London, London, United Kingdom.
Email: p.slator@ucl.ac.uk

Funding information

National Institutes of Health (NIH), Grant/Award Number: 1U01HD087202-01; Wellcome Trust, Grant/Award Number: 201374/Z/16/Z; EPSRC, Grant/Award Number: N018702, M020533 and EP/N018702/1; National Institute for Health Research (NIHR), Grant/Award Number: RP-2014-05-019; Tommy's Charity; Holbeck Charitable Trust

Purpose: A combined diffusion-relaxometry MR acquisition and analysis pipeline for in vivo human placenta, which allows for exploration of coupling between T_2^* and apparent diffusion coefficient (ADC) measurements in a sub 10-minute scan time.

Methods: We present a novel acquisition combining a diffusion prepared spin echo with subsequent gradient echoes. The placentas of 17 pregnant women were scanned in vivo, including both healthy controls and participants with various pregnancy complications. We estimate the joint T_2^* -ADC spectra using an inverse Laplace transform.

Results: T_2^* -ADC spectra demonstrate clear quantitative separation between normal and dysfunctional placentas.

Conclusions: Combined T_2^* -diffusivity MRI is promising for assessing fetal and maternal health during pregnancy. The T_2^* -ADC spectrum potentially provides additional information on tissue microstructure, compared to measuring these two contrasts separately. The presented method is immediately applicable to the study of other organs.

KEYWORDS

diffusion, inverse Laplace transform, placenta, microstructure, multimodal MRI, relaxometry

1 | INTRODUCTION

The placenta provides the vital link between mother and fetus during pregnancy. It is implicated in many major pregnancy complications, such as pre-eclampsia (PE) and fetal

growth restriction (FGR).¹ PE affects 3–5% of pregnancies² and is a major cause of maternal and perinatal mortality.^{3,4} Late onset FGR, defined as that diagnosed after 32 weeks,⁵ affects 5–10% of pregnancies.⁶ It is strongly associated with stillbirth,^{7,8} pre-eclampsia,⁹ and late preterm birth.¹⁰ For all

*Paddy J. Slator and Jana Hutter contributed equally to this work.

these disorders, it is likely that placental dysfunction occurs before the onset of symptoms. New techniques for imaging the placenta therefore have the potential to improve prediction, diagnosis, and monitoring of pregnancy complications.

Placental MRI is emerging as a technique with substantial promise to overcome some disadvantages of ultrasound. For example, ultrasound parameters of fetal wellbeing are imperfect for determining which fetuses have late-onset FGR and are at greatest risk of adverse perinatal outcome, as opposed to those that are constitutionally small but healthy.^{6,11} Assessing the placenta with MRI has the potential to make this distinction. Two MRI modalities that show great promise for assessing placental function are T_2^* relaxometry—which has the potential to estimate oxygenation levels,^{12,13} and diffusion MRI (dMRI)—which can estimate the microstructure and microcirculatory properties.¹⁴⁻¹⁷

T_2^* relaxometry exploits the inherent sensitivity of the transverse relaxation time to the biochemical environment of tissue. In particular, the paramagnetic properties of hemoglobin mean that the T_2^* time constant can be used as a proxy estimation of oxygenation.¹⁸ In placental studies, T_2^* is generally lower in FGR cases.¹⁹⁻²² A typical experiment acquires gradient echo data at several echo times (TE), either in separate or multi-echo scans, and hence estimates the T_2^* constant of the tissue. No diffusion weighting is typically applied to these scans. Applying diffusion gradients with different strengths (*b*-value) and directions provides sensitivity to various microstructural length scales and orientations. These measurements are usually taken at a fixed TE. In the placenta, dMRI has shown promise for discrimination between normal pregnancies and FGR,^{14,15,23-26} and early onset PE.¹⁶ However, despite the large number of placental T_2^* and dMRI studies in the literature, no method has shown sufficient discrimination between healthy pregnancies and those with complications to be introduced into routine clinical practice. Methods which combine multiple distinct measurements may provide a way to overcome this. Supporting Information Table S1 summarizes T_2^* and dMRI studies in the placenta to date.

T_2^* and dMRI-derived measures are both influenced by the presence and composition of distinct tissue compartments (or *microenvironments*). Diffusion-relaxometry MRI can simultaneously measure multiple MR contrasts; for example, by varying both TE and *b*-value it is possible to probe the multidimensional T_2 -diffusivity (or T_2^* -diffusivity) space. MR experiments dating back to the 1990s have simultaneously measured diffusivity and T_2 ²⁷⁻³¹; such experiments are often categorized as diffusion-relaxation correlation spectroscopy (DRCOSY).³² These acquisitions naturally pair with multidimensional analysis techniques which quantify multiple tissue parameters simultaneously, and therefore have great potential to yield fine-grained information on tissue microstructure. Such analysis techniques have been recently applied to

combined diffusion-relaxometry experiments in the context of nuclear magnetic resonance (NMR) spectroscopy, improving the ability to distinguish different compartments.^{33,34} Recent work applying these techniques to imaging has applications in the T_1 -diffusivity,³⁵ T_2 -diffusivity,^{36,37} and T_1 - T_2 -diffusivity³⁸ domains. These studies have shown that combining diffusion with other MR contrasts leads to more specific quantification of microscopic tissue compartments. One recent study demonstrated combined T_2 -diffusivity in the placenta,³⁹ with the aim to separate signals from fetal and maternal circulations.

A major disadvantage of previous diffusion-relaxometry experiments are the very long scan times required when varying multiple contrast mechanisms, such as the TE and diffusion encoding. In this paper, we propose a combined acquisition and analysis technique which can estimate the T_2^* -ADC spectrum within a clinically viable timeframe. We apply this novel method in the placenta, an organ where T_2^* and ADC have both been shown to be informative. As well as demonstrating simultaneous estimation of T_2^* and diffusivity parameters within a clinically viable time, we hypothesize that the joint T_2^* -ADC spectrum will provide additional information compared to the individual measures.

2 | METHODS

2.1 | Acquisition: Integrated T_2^* -Diffusion sampling

We adapt a novel MRI acquisition strategy, termed ZEBRA,⁴⁰ in order to sample multiple TEs and diffusion encodings within a single repetition time (TR). The method combines a diffusion prepared spin echo sequence with subsequent gradient echoes. This allows simultaneous quantification of T_2^* and ADC, as opposed to standard independent multi-echo gradient echo and diffusion sequences (e.g. Figure 1A). Our technique also offers significant speed ups compared to existing T_2 -diffusivity techniques—which only sample a single TE-diffusion encoding pair for each TR (i.e. Figure 1A). The proposed combined acquisition is shown in Figure 1B. The multiple gradient echoes are acquired with minimal spacing after the initial spin echo and diffusion preparation. We note that using gradient echo readouts rather than spin echoes, we measure T_2^* rather than T_2 (see Figure 1C).

Figure 2 illustrates the resultant sampling of the TE-diffusion encoding domain for the three acquisition techniques presented in Figure 1. Separate multi-echo gradient echo and diffusion sequences do not adequately sample the full domain (Figure 2A). With repeat acquisitions of diffusion encodings at different TEs full sampling of the domain is possible, but very slow (Figure 2B). The proposed acquisition is able to sample the same domain in a much shorter, and clinically viable, scanning time (i.e. Figure 2C).

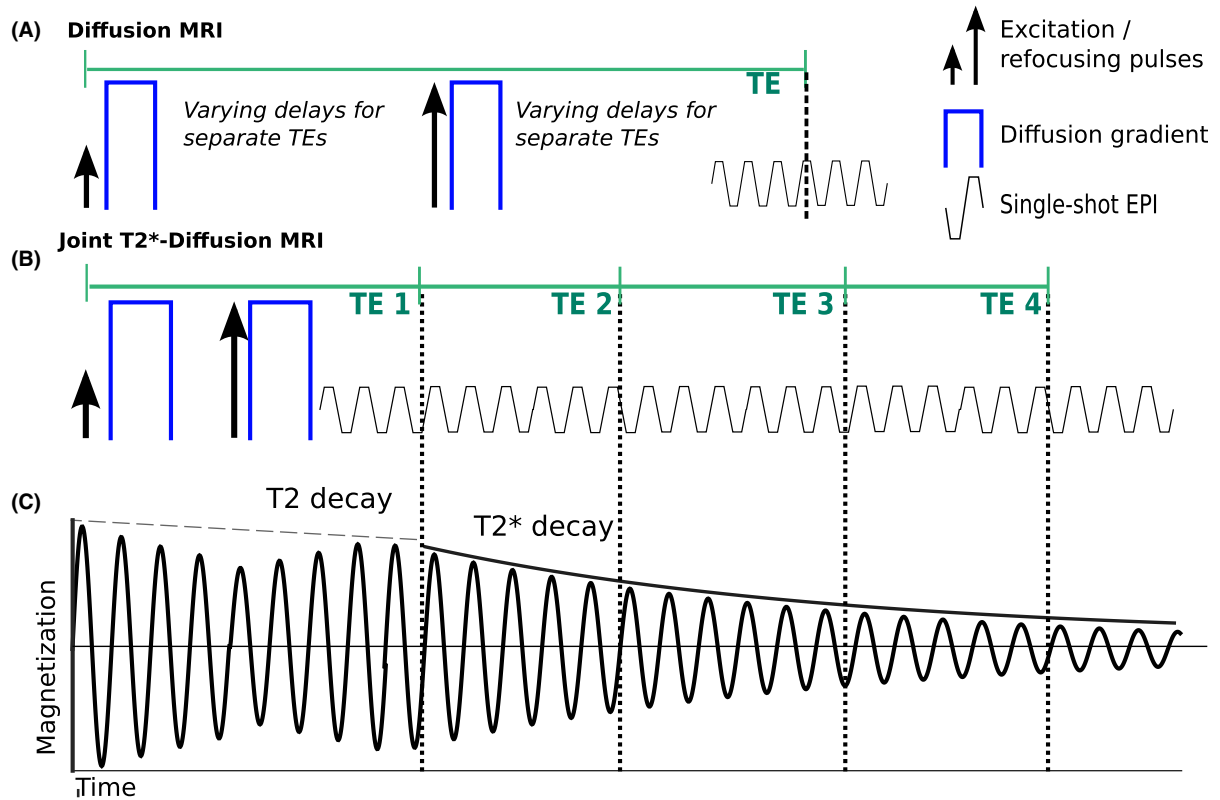


FIGURE 1 The considered acquisition schemes. A, Conventional Diffusion MRI acquisition for one echo time (TE) showing the diffusion gradients (blue), the excitation and refocusing pulses as well as the single-shot EPI readout train. Repeating this acquisition with varying delays between the diffusion gradients and the readout leads to different TE s and thus combined T_2 -diffusion MRI. B, Proposed combined acquisition with an initial spin echo acquired after the diffusion gradients followed by multiple Gradient echos. C, Magnetization for the combined acquisition, with both T_2 and T_2^* decay. The signal evolution neglects effects of all applied gradients

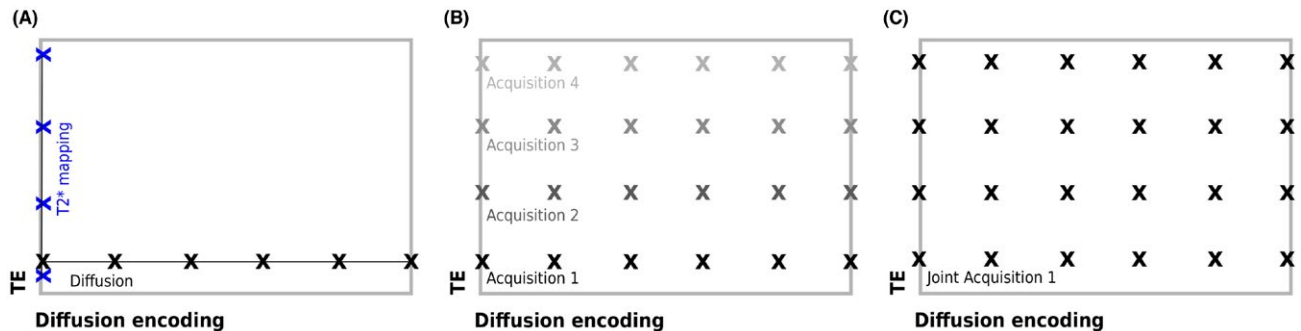


FIGURE 2 Schemes for the three considered diffusion-relaxometry experiments illustrated in the TE -diffusion encoding acquisition parameter plane. A, Schematic of conventional separate T_2^* mapping and diffusion MRI showing the encoding of different echo times for $b = 0$ in blue and different diffusion encoding settings at fixed echo time. B, Parameter space illustrating the sampling of the TE -diffusivity space with diffusion acquisitions at several TE s. Shading illustrates separate diffusion acquisitions at fixed TE s. C, Proposed combined T_2^* -diffusion acquisition illustrating a denser sampling scheme achieved in a single acquisition

2.2 | Modeling

The simplest model for analyzing the data considers single-tissue compartments, so that the signal attenuations caused by T_2^* relaxation and diffusion are both assumed to give rise to a single-exponential decay. The MR signal for this combined ADC - T_2^* model is given by

$$S(T_E, b) = S_0 e^{-T_E/T_2^*} e^{-bADC} \quad (1)$$

where T_E is the echo time, b is the b -value, ADC is the apparent diffusion coefficient, T_2^* is the effective transverse relaxation time, and S_0 is the signal at the spin echo time with zero diffusion weighting. S_0 is the product of proton density, T_2 weighting caused by finite spin echo time, receiver coil

properties, and system gain, so we do not treat it as an absolute quantity in the analysis.

A shortcoming of this model is that it assumes the attenuation due to diffusion is monoexponential, when it is well established that the placental dMRI signal in vivo is at least biexponential, as in the intravoxel incoherent motion (IVIM) model.⁴¹ In this model, the slow and fast attenuating components are associated with diffusion in tissue and pseudo-diffusion in capillaries, respectively. Incorporating T_2^* decay into the IVIM model gives

$$S(T_E, b) = S_0 e^{-T_E/T_2^*} [f e^{-bD^*} + (1-f) e^{-bADC}] \quad (2)$$

where f is the perfusion fraction and D^* is the pseudo-diffusion coefficient. However, it seems likely that the diffusion and pseudo-diffusion compartments have different T_2^* values. A model incorporating this was proposed by Jerome et al⁴²

$$S(T_E, b) = S_0 \left[f e^{-bD^*} e^{-T_E/T_{2p}^*} + (1-f) e^{-bADC} e^{-T_E/T_2^*} \right] \quad (3)$$

where T_{2p}^* and T_2^* are the T_2^* values specific to the pseudo-diffusion and diffusion monoexponential signal components, respectively.

A significant limitation of the models presented in Equations (1)–(3) is that the number of signal components is assumed to be known. An alternative approach for analyzing the signal is a continuum model, which considers that spins have a spectrum of relaxivity (or diffusivity) values all contributing to the MRI signal. Following Menon et al⁴³, the 1D continuum models for T_2^* relaxometry and diffusion are

$$\begin{aligned} S(T_E) &= \int p(T_2^*) e^{-T_E/T_2^*} dT_2^* \\ S(b) &= S_0 \int p(ADC) e^{-bADC} dADC. \end{aligned}$$

Here $p(T_2^*)$ and $p(ADC)$ are the T_2^* relaxation and diffusivity spectra to be estimated from the data. We can solve for these spectra using an inverse Laplace transformation, although this is an ill-posed problem requiring regularization to smooth the resulting spectra.^{36,38,44-46} The extension to combined diffusion-relaxometry acquisitions is simple. For the acquisition presented here, where T_E and b are simultaneously varied, the signal is (e.g.⁴⁷)

$$S(T_E, b) = S_0 \int_0^\infty p(T_2^*, ADC) e^{-TE/T_2^*} e^{-bADC} dT_2^* dADC \quad (4)$$

The function we are interested in is the two-dimensional T_2^* -diffusivity spectrum, $p(T_2^*, ADC)$, which can be estimated by a regularized 2D inverse Laplace transform. This contains more information than the individual 1D spectra, and is hence more likely to resolve multiple distinct tissue compartments. Although we emphasize that, due to choice of kernels in the continuum models, these distinct compartments—that

is, separate peaks in 2D spectra—are assumed to be the result of monoexponential signal decays.

2.3 | Experiments

The sequence described in the methods section was implemented on a clinical Philips Achieva-Tx 3T scanner using the 32ch adult cardiac coil placed around the participant's abdomen for signal reception. All methods were carried out in accordance with relevant guidelines and regulations; the study was approved by the Riverside Research Ethics Committee (REC 14/LO/1169) and informed written consent was obtained prior to imaging. Seventeen pregnant women, with gestational age ranging from 23+5 to 35+4 (weeks + days), were successfully scanned using the described technique. Three of these participants, one of whom also had FGR, were diagnosed with pre-eclampsia according to standard definitions.⁴⁸ Three participants had chronic hypertension in pregnancy and were analyzed distinct from normotensive pregnancy women (the control group). One pregnant woman with chronic hypertension was scanned twice, 4 weeks apart, and developed superimposed pre-eclampsia by the second scan. The full participant details are given in Table 1.

The combined T_2^* -diffusivity scan was acquired with the proposed sequence, a dMRI prepared spin echo followed by multiple gradient echos. The number and timing of the gradient echos varied across scans (see Table 1), with most scans having five TEs. The diffusion encodings were chosen specifically for the placenta, as previously reported,^{49,50} with three diffusion gradient directions at $b = [5, 10, 25, 50, 100, 200, 400, 600, 1200, 1600]$ s mm⁻², eight directions at $b = 18$ s mm⁻², seven at $b = 36$ s mm⁻², and 15 at $b = 800$ s mm⁻². Further parameters were FOV = 300 × 320 × 84 mm, TR = 7 s, SENSE = 2.5, halfscan = 0.6, resolution = 3 mm³. One participant was scanned at higher resolution: 2 mm isotropic. The total acquisition time was 8 minutes 30 seconds. We acquired all images coronally to the mother. Attempting to acquire images in the same plane relative to the placenta would be very difficult, due to the heterogeneity in placental positioning and curvature across subjects. In clinical practice, the imaging plane with respect to the placenta has to vary widely; our samples allow us to demonstrate the method across a range of orientations. Supporting Information Figure S2 displays raw data from a single acquisition.

2.4 | Model fitting

We first manually defined a region of interest (ROI) containing the whole placenta and adjacent uterine wall section on the first $b = 0$ image with the lowest TE. We fit the T_2^* -ADC model described in Equation (1) voxelwise to the data (all TEs and all b -values). The fitting consisted of two-step (grid search followed by gradient descent) maximum

log-likelihood estimation assuming Rician noise, similar to that previously described,¹⁷ with the exception that we use the unnormalized MRI signal. The gradient descent fitting constraints were as follows: T_2^* was constrained between 0.001 seconds and 1 second, the ADC between 10^{-5} and $1 \text{ mm}^2 \text{ s}^{-1}$, and S_0 between 0.001 and 10^5 . We fixed the SNR for fitting to 20 for all voxels in all scans.

We calculated the T_2^* -ADC spectrum for each participant from the signal averaged over the ROIs, using the MERA toolbox,⁵¹ which incorporates minimum amplitude energy regularization as described by Whittall et al.⁵² We also calculated the T_2^* -ADC spectra voxelwise in all participants. We next quantified the spatial variation in T_2^* -ADC spectral components across the placenta and uterine wall with volume fraction maps, using a similar approach to Benjamini et al.³⁸ and Kim et al.³⁶ Specifically, by inspecting the ROI-averaged spectra we chose a set of boundaries—based on the most common peak areas—which split the T_2^* -ADC domain into regions. These boundaries were the same across all participants, and are given in Table 2. For each voxel's T_2^* -ADC spectrum, we then calculated the weight of the voxelwise spectra contained in each of these regions. By normalizing these weights to sum to 1 across all regions, we produced spectral volume fraction estimates for each voxel. Figure 3 shows an illustrative example of this calculation; the spectral volume fraction essentially quantifies the proportion of each voxel's spectrum which lies in each of the highlighted regions in the top-left panel.

3 | RESULTS

Figure 3 demonstrates the full analysis pipeline output for a single participant. We next present the parameter maps from combined ADC- T_2^* model fits (Figures 4 and 5) and spectral volume fraction maps (Supporting Information Figures S4-S6) for all participants. We probe the changes across gestation and in disease cases by examining the T_2^* -ADC spectra across all participants (Figures 6 and 7). Finally, in order to assess the independence of our diffusivity and relaxometry measurements, we plot the correlation between the derived ADC and T_2^* values (Supporting Information Figure S6).

The first panel in Figure 3 shows the placenta and uterine wall ROI averaged T_2^* -ADC spectrum for a single participant (scanned at higher resolution). We observe three peaks, clearly separated by ADC value but with similar T_2^* values. ADC and T_2^* maps show distinctive spatial patterns. The ADC is much higher in the uterine wall than the placenta. T_2^* maps show distinct “lobes” surrounded by a patchwork of low T_2^* values, with many lobes displaying a small region of higher T_2^* in the center. The bottom row of Figure 3 displays voxelwise spectral volume fractions, obtained by integrating (i.e. summing spectral weights)

TABLE 1 Participant details

Participant ID	GA at scan (weeks)	Cohort	TEs (ms)
1	23.72	Control	78, 114, 150, 186, 222
2	23.86	Control	78, 114, 150, 186, 222
3	25.43	Control	78, 114, 150, 186, 222
4	25.72	Control	78, 114, 150, 186, 222
5	26.14	Control	78, 114, 150, 186, 222
6	26.72	Control	78, 114, 150, 186
7	26.72	Control	78, 114, 150, 186, 222
8	27.14	Control	78, 114, 150, 186, 222
9	28.29	Control	78, 114, 150, 186, 222
10	28.86	Control	82, 175, 268, 361, 454
11	28.86	Control	78, 114, 150, 186, 222
12	29.67	Control	85, 145, 205, 265, 325
13	26.86	CH	80, 121, 162, 203, 245
14	34.43	CH	78, 114, 150, 186, 222
15	27.7	PE+FGR	78, 114, 150, 186, 222
16	30.58	PE	78, 114, 150
17 (scan 1)	30.71	CH	78, 114, 150, 186, 222
17 (scan 2)	34.14	CH+PE	78, 114, 150, 186, 222

Abbreviations: PE, pre-eclampsia; CH, chronic hypertensive; FGR, fetal growth restriction.

TABLE 2 Boundaries selected to segregate most common peak areas in T_2^* -ADC spectra

Region	ADC Bounds ($\times 10^{-3} \text{ mm}^2 \text{ s}^{-1}$)	T_2^* Bounds (s)
Peak 1	$0 < ADC < 25$	$0 < T_2^* < 0.1$
Peak 2	$25 < ADC < 200$	$0 < T_2^* < 0.1$
Peak 3	$200 < ADC < 1000$	$0 < T_2^* < 0.1$

within three regions of the T_2^* -ADC space, as described in Methods. The domain with the lowest ADC (e.g. peak 1) is associated with areas within the placenta, and the two domains (peaks 2 and 3) with higher ADC are more prominent in the uterine wall.

Figure 4 shows T_2^* maps across all participants from the combined T_2^* -ADC fit. The patterns are consistent with those previously reported in the literature.^{50,53} In most participants regions of high T_2^* encircled by low T_2^* borders are clearly visible, and most likely correspond to placental lobules, with high T_2^* indicating the presence of oxygenated blood. In agreement with previous observations, the regions with low T_2^* are more prominent in pre-eclampsia,⁵⁰ and FGR^{22,54} placentas.

ADC maps (Figure 5) also show anatomically linked qualitative features which are consistent across participants. In all scans from the healthy pregnant group the, ADC shows a significant increase at the border between the placenta and

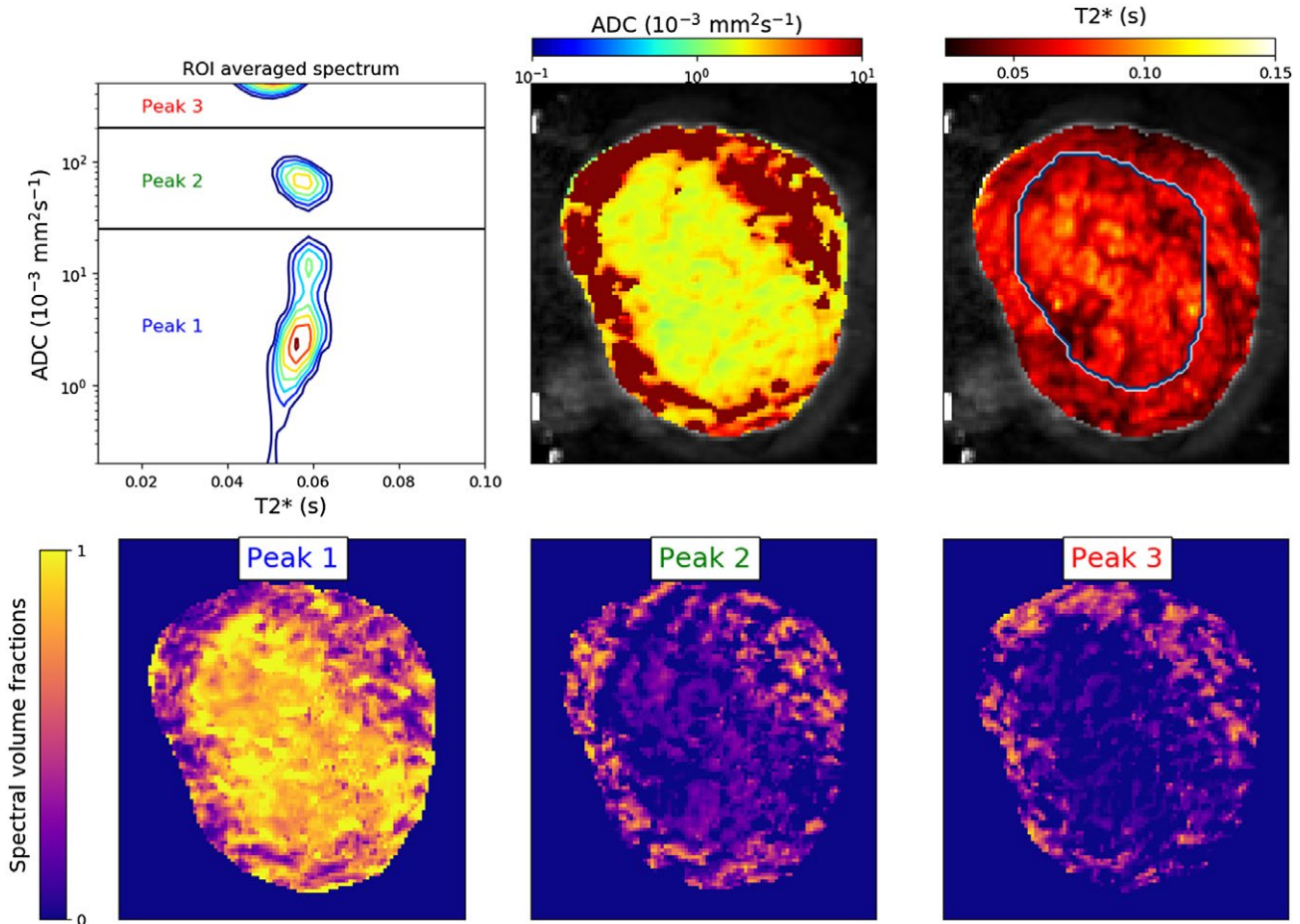


FIGURE 3 T_2^* -ADC spectra show anatomical specificity. Spatial maps for a single scan with higher resolution. Top row: T_2^* -ADC spectrum derived from inverse Laplace transforms of the spatially averaged signal within an ROI comprising the entire placenta and uterine wall, and ADC and T_2^* maps from combined T_2^* -ADC fit. The manually defined placenta ROI is outlined in the T_2^* map. Bottom row, spectral volume fraction maps derived by summing the weight of the spectra in the three domains displayed in the ROI averaged spectrum, as described in Methods

the uterine wall. This is most likely explained by the high levels of blood flow in these areas. This bordering area of high ADC is absent from many disease placentas. Additionally, placentas from women with chronic hypertension and preeclampsia often show a distinctive pattern—small patches of high ADC surrounded by very low ADC.

Figure 6 displays the spatially averaged T_2^* -ADC spectra for ROIs containing the placenta and uterine wall. We clearly observe separate peaks in all control participants, strongly suggesting the presence of multiple tissue compartments with distinct properties. In the vast majority (11/12) of these spectra from healthy controls, we see at least three clearly separated peaks. The ADC values of two of these peaks are typically above the diffusivity of water in free media (Figure 6, blue dashed lines), suggesting multiple microenvironments with different incoherent flow speeds. These peaks, and their corresponding tissue compartments, appear more clearly separated by ADC (note the log-scale on the y-axis) than by T_2^* value. We also observed three distinct peaks in placentas from chronic hypertensive women. Interestingly, we did not

see three distinct peaks in any spectra from participants with pregnancy complications (three PE, one PE+FGR). There is a distinct pattern in the T_2^* -ADC spectra for the three PE participants—a left and downward shift in the lowest peak. This suggests a decrease in both ADC and T_2^* distributions compared to control placentas. There is a similar leftward shift in the PE+FGR placental spectrum; however, the downward shift is not as pronounced, with the middle peak appearing to merge with the lowest peak. The peak with the highest ADC often appears to span the boundary of the domain in which the inverse Laplace transform is calculated. This is likely because we are unable to sample enough low b -values to accurately estimate this very fast diffusing component—i.e. there is signal in the $b = 0$ volume, which has all attenuated by the $b = 5$ s mm⁻² volume.

Spectral volume fraction maps showed similar patterns across all control participants (Supporting Information Figures S3-S5); peaks with higher ADC being more prominent in the uterine wall. This likely reflects the high flowing blood volumes in these areas, akin to the maps in Figure 5.

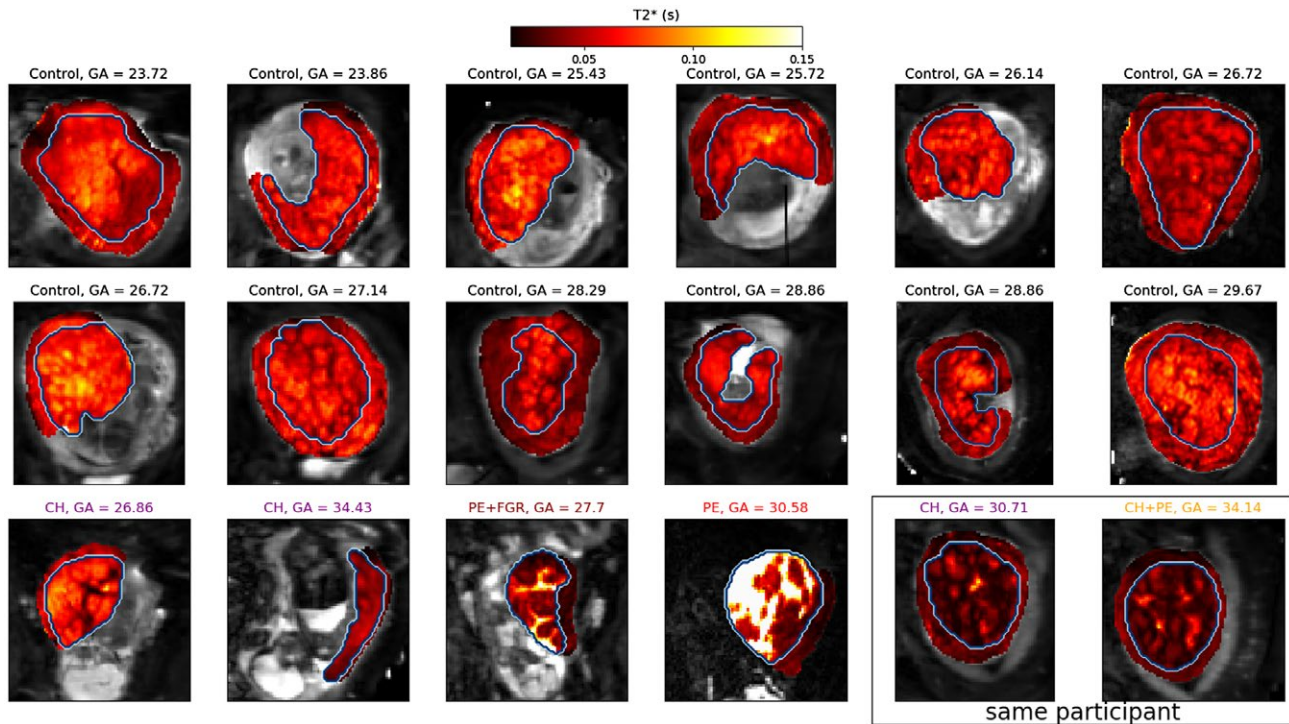


FIGURE 4 T_2^* maps from combined ADC- T_2^* fit. Participants with pregnancy complications in color. The manually defined placenta ROI is outlined. Note the very high T_2^* values for the GA = 30.58 participant—this is very likely due to model fitting failure caused by very low signal in this placenta

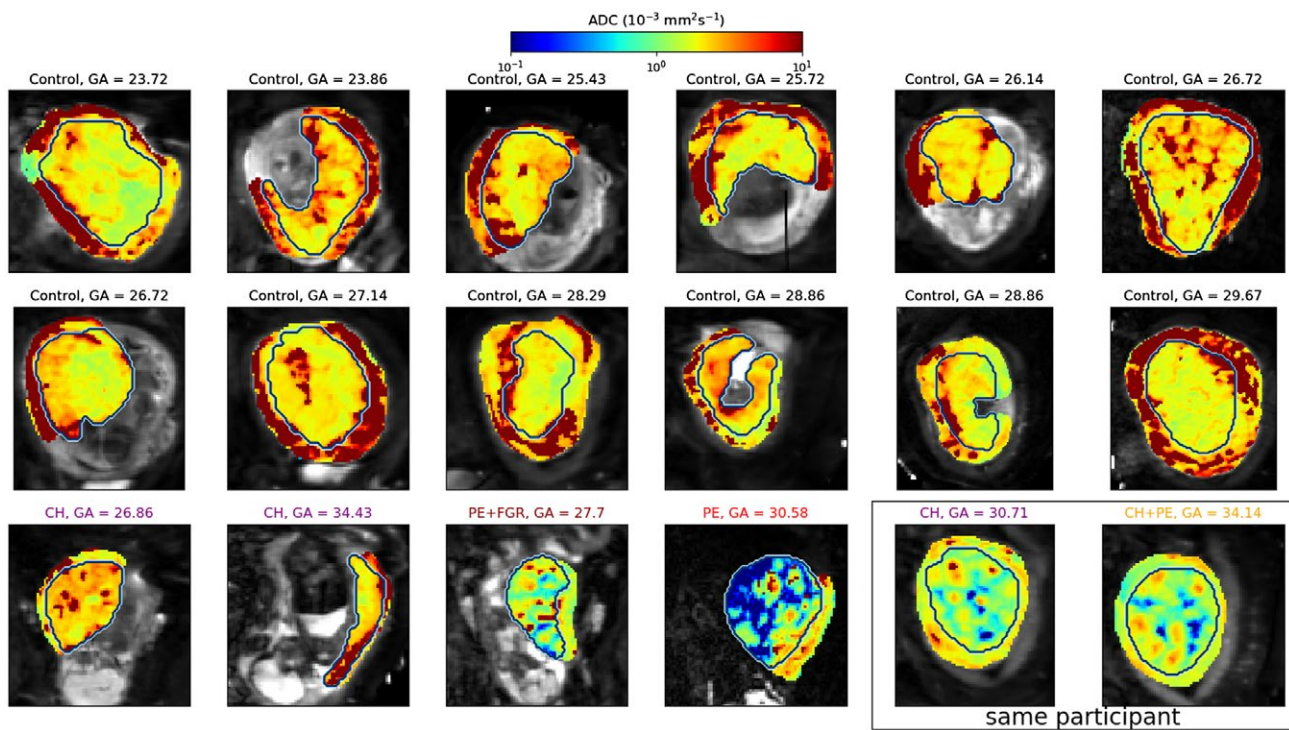


FIGURE 5 ADC maps from combined ADC- T_2^* fit. The manually defined placenta ROI is outlined. Note the log-scale colormap

Supporting Information Figure S6 shows that we did not observe a consistent correlation between T_2^* and ADC values across participants. This suggests that we acquire

complementary information from these two MR contrasts. Interestingly, we did not observe the small placental areas with high T_2^* and high ADC that we saw in previous work.⁵⁰

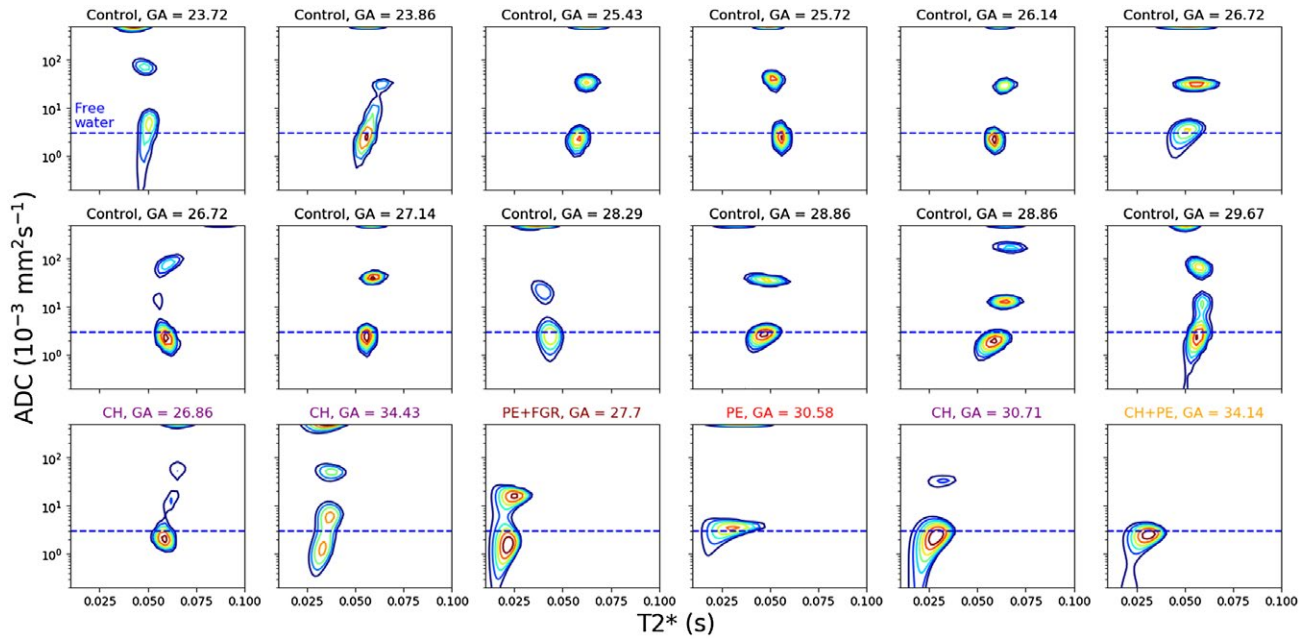


FIGURE 6 T_2^* -ADC spectra derived from inverse Laplace transforms of the spatially averaged signal within placenta and uterine wall ROIs. Horizontal dashed blue lines represent the approximate diffusivity of water in free media at 37°C ($3 \times 10^{-3} \text{ mm}^2 \text{ s}^{-1}$)

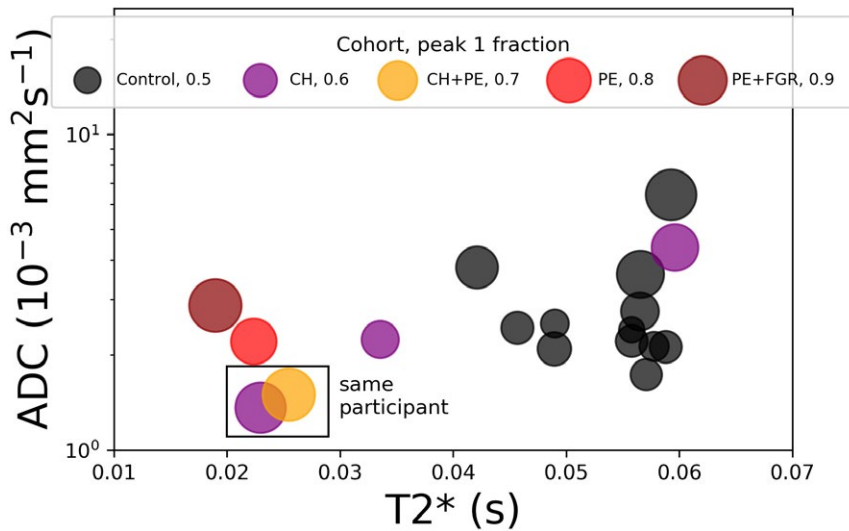


FIGURE 7 Position of the peak with the lowest ADC within the ADC- T_2^* spectrum. Each marker corresponds to a single scan. Markers are colored by disease cohort, and marker area is proportional to the spectral volume fraction of the peak

4 | DISCUSSION AND CONCLUSION

4.1 | Summary

This study demonstrates accelerated diffusion-relaxometry MRI on the in vivo human placenta. Compared to existing approaches, it allows denser, faster, and more flexible sampling of the 2D (TE—diffusion encoding) acquisition space. This in turn allows visualization of the T_2^* -ADC spectrum, and thus provides enhanced capacity to separate multiple tissue microenvironments. The technique was demonstrated on 17 pregnant participants, including 3 scans on placentas clinically assessed as from women with pregnancy complications.

In the following sections, we first putatively associate the observed T_2^* -diffusivity spectral peaks with distinct placental tissue microenvironments. We then hypothesize as to how the spectral changes observed in cases with complications reflect changes in these tissue microenvironments. Finally, we discuss the clinical potential of the presented technique, which we emphasize is independent of the biological interpretation.

4.2 | Biological interpretation of T_2^* -diffusivity spectra

In all controls, we observed a peak with high ADC, typically above $10^{-1} \text{ mm}^2 \text{ s}^{-1}$. Additionally, in nearly every control

participant (11/12) we observe two further clearly distinct peaks, with ADC around $2 \times 10^{-3} \text{ mm}^2 \text{ s}^{-1}$ for the lower, and between 10^{-2} and $10^{-1} \text{ mm}^2 \text{ s}^{-1}$ for the middle peak (Figure 6).

The appearance of three peaks clearly separated by diffusivity in all but one control placenta is consistent with each peak corresponding to a distinct placental tissue microdomain. Solomon et al. previously reported three placental compartments in mice,⁵⁵ with these attributed to a slow-diffusing maternal blood compartment, a fetal blood compartment with diffusivity around two orders of magnitude faster, and an intermediate compartment associated with active filtration of fluid across the fetal-maternal barrier. We therefore speculatively assign tissue compartments to each of these three peaks in healthy control placentas as follows. The compartment with the lowest ADC, which has typical values ($2 \times 10^{-3} \text{ mm}^2 \text{ s}^{-1}$) comparable to the diffusivity of water in tissue, is associated with water which is not subject to significant incoherent flow effects—this may be within tissue or slow-moving maternal blood. The highest ADC compartment is associated with perfusing fetal blood, and the intermediate compartment with fluid transitioning between the maternal and fetal circulations—a significant proportion of which may reside within tissue. This is consistent with the spectral volume fraction maps for the peaks with higher ADC (Supporting Information Figures S4 and S5), which show higher intensity in the vascular areas bordering the placenta. The accuracy of these speculative tissue compartment assignments could be tested by comparison with *ex vivo* histology. Although such comparisons are notoriously challenging, achieving detailed correspondence would be highly valuable.

4.3 | Spectral changes in disease

We observed three main trends in the T_2^* -diffusivity spectrum which discriminated between control and placentas from women with pregnancy complications:

1. The disappearance of one (or both) of the middle and higher peaks
2. The lowest peak has a lower T_2^*
3. The lowest peak has a lower diffusivity

In placentas from women with pre-eclampsia, we generally saw all three trends (Figure 6). The lower T_2^* mirrors the previously reported decrease in T_2^* in pre-eclampsia placentas.⁵⁰ We saw the same trend in the FGR+PE case, and note that lower T_2^* values have also been observed in FGR placentas.^{22,56} Regarding the lower diffusivity in the lowest peak, our initial speculation is that this could reflect increased water restriction due to inflammation—since placental inflammation is associated with PE.⁵⁷ This may relate to the disappearance of the middle peak, which we hypothesis could reflect decreased

maternal-fetal fluid exchange. Inflammation is a potential mechanism facilitating the reduction in exchange, although we emphasize that this speculative link can only be confirmed (or refuted) by comparison with postdelivery histology. Figure 7 presents these observed changes in the T_2^* -ADC spectrum in a single plot, showing clear separation between the control and pregnancy complication (i.e. PE, PE+FGR) participants. We plot the position of the spectral peak with the lowest ADC in the T_2^* -ADC domain, with the marker area corresponding to the peak's volume fraction. In this way, we capture both the peak shift, and the higher volume fraction due to the disappearance of the middle or higher peaks. Although these results are highly encouraging, we clearly need to scan many more participants, both control and women with pregnancy complications, to determine the discriminative power of these measures.

4.3.1 | Limitations and future work

We used an “out-of-the-box” inverse Laplace transform toolbox to calculate the T_2^* -ADC spectrum. There are a number of known weaknesses for this method, including the need for regularization. In this study, we chose minimum amplitude energy regularization. Future work could assess the utility of alternative optimization approaches, such as spatially constrained,³⁶ or constrained by the 1D spectra.³⁸

Our T_2^* estimates are generally lower than those previously reported.⁵⁰ This may be due to the larger voxel size, leading to partial volume effects around areas with high T_2^* , such as spiral artery inlets. It could also be due to signal attenuation due to diffusion during the gradient echoes, something which we did not account for in our analysis.

The presented T_2^* -ADC spectral analysis assesses the data in two dimensions, but there are more dimensions to the data—such as diffusion gradient direction—which we did not include in our analysis. Therefore, this data set has the potential to be further analyzed, for example, with microstructural models that account for anisotropy in the signal.

In this study, we used *b*-values and gradient directions optimized for dMRI at a single TE,^{50,58} and the TEs were constrained by the EPI readout train length. Separate optimization of T_2^* relaxometry and dMRI acquisition parameters is 1D (choice of TEs, choice of *b*-values). However, when moving to combined T_2^* -diffusion this becomes a 2D problem—for example, in the isotropic case we need to choose optimal TE-diffusion encoding pairs. In future, we plan to optimize these TE-diffusion encoding values in order to give the best sampling of the 2D parameter space, and enhance estimation of the 2D spectra.

4.4 | Outlook and clinical application

The combined acquisition and analysis technique presented here offers the fast, simultaneous, and multidimensional

assessment of placental T_2^* and diffusivity in less than 10 minutes. These two MR contrasts have been shown elsewhere to be sensitive to placental pathologies, we hypothesize that their simultaneous assessment could enable better separation of healthy and poorly functioning placentas. This is supported by the fact that we did not see consistent correlation between T_2^* and ADC values (Supporting Information Figure S6), suggesting that these modalities offer complementary information. This reinforces the value of the novel technique presented here as a quantitative tool for assessment of pregnancy complications, with the potential to ultimately inform clinical decisions. Furthermore, we believe that fast calculation of the T_2^* -ADC spectrum has many potential applications in other areas of biomedical research.

ACKNOWLEDGMENTS

We thank the midwives, obstetricians, and radiographers who played a key role in obtaining the data sets. We would also like to thank all participating mothers.

ORCID

Paddy J. Slator  <http://orcid.org/0000-0001-6967-989X>

REFERENCES

- Brosens I, Pijnenborg R, Vercruyse L, Romero R. The "Great Obstetrical Syndromes" are associated with disorders of deep placentation. *Am J Obstetrics Gynecol.* 2011;204:193–201.
- Mol BWJ, Roberts CT, Thangaratinam S, Magee LA, de Groot CJM, Hofmeyr GJ. Pre-eclampsia. *The Lancet* 2016;387:999–1011.
- Duley L. The global impact of pre-eclampsia and Eclampsia. *Seminars Perinatol.* 2009;33:130–137.
- Say L, Chou D, Gemmill A, et al. Global causes of maternal death: a WHO systematic analysis. *The Lancet Global Health* 2014;2:e323–e333.
- Gordijn SJ, Beune IM, Thilaganathan B, et al. Consensus definition of fetal growth restriction: a Delphi procedure. *Ultrasound Obstetrics Gynecol.* 2016;48:333–339.
- Figueras F, Caradeux J, Crispi F, Eixarch E, Peguero A, Gratacos E. Diagnosis and surveillance of late-onset fetal growth restriction. *Am J Obstetrics Gynecol.* 2018;218:S790–S802.e1.
- Gardosi J, Madurasinghe V, Williams M, Malik A, Francis A. Maternal and fetal risk factors for stillbirth: population based study. *British Med J.* 2013;346:f108.
- Bukowski R, Hansen NI, Pinar H, et al. Altered fetal growth, placental abnormalities, and stillbirth. *PLOS ONE* 2017;12:e0182874.
- Srinivas SK, Edlow AG, Neff PM, Sammel MD, Andrela CM, Elovitz MA. Rethinking IUGR in preeclampsia: dependent or independent of maternal hypertension? *J Perinatol.* 2009;29:680–684.
- Loftin RW, Habli M, Snyder CC, Cormier CM, Lewis DF, DeFranco EA. Late preterm birth. *Rev Obstetrics Gynecol.* 2010;3:10–9.
- MacDonald TM, McCarthy EA, Walker SP. Shining light in dark corners: Diagnosis and management of late-onset fetal growth restriction. *Aus N Zeal J Obstet Gynaecol.* 2015;55:3–10.
- Huen I, Wright C, Parker G, Sibley C, Johnstone E, Naish J. R_1 and R_2^* changes in the human placenta in response to maternal oxygen challenge. *Magn Reson Med.* 2013;70:1427–1433.
- Sørensen A, Peters D, Fründ E, Lingman G, Christiansen O, Ulbjerg N. Changes in human placental oxygenation during maternal hyperoxia estimated by blood oxygen level-dependent magnetic resonance imaging (BOLD MRI). *Ultrasound Obstetrics Gynecol.* 2013;42:310–314.
- Moore RJ, Strachan BK, Tyler DJ, et al. In utero perfusing fraction maps in normal and growth restricted pregnancy measured using IVIM echo-planar MRI. *Placenta* 2000;21:726–732.
- Derwig I, Lythgoe DJ, Barker GJ, et al. Association of placental perfusion, as assessed by magnetic resonance imaging and uterine artery Doppler ultrasound, and its relationship to pregnancy outcome. *Placenta* 2013;34:885–891.
- Sohlberg S, Mulic-Lutvica A, Lindgren P, Ortiz-Nieto F, Wikström AK, Wikström J. Placental perfusion in normal pregnancy and early and late preeclampsia: a magnetic resonance imaging study. *Placenta* 2014;35:202–206.
- Slator PJ, Hutter J, McCabe L, et al. Placenta microstructure and microcirculation imaging with diffusion MRI. *Magn Reson Med.* 2018;80:756–766.
- Zhao JM, Clingman CS, Närväinen MJ, Kauppinen RA, Van Zijl PCM. Oxygenation and hematocrit dependence of transverse relaxation rates of blood at 3T. *Magn Reson Med.* 2007;58:592–597.
- Sinding M, Peters DA, Frøkjær JB, et al. Prediction of low birth weight: comparison of placental T_2^* estimated by MRI and uterine artery pulsatility index. *Placenta* 2017;49:48–54.
- Ingram E, Morris D, Naish J, Myers J, Johnstone E. MR imaging measurements of altered placental oxygenation in pregnancies complicated by fetal growth restriction. *Radiology* 2017;285:953–960.
- Derwig I, Barker GJ, Poon L, et al. Association of placental T_2 relaxation times and uterine artery Doppler ultrasound measures of placental blood flow. *Placenta* 2013;34:474–479.
- Sinding M, Peters DA, Poulsen SS, et al. Placental baseline conditions modulate the hyperoxic BOLD-MRI response. *Placenta* 2018;61:17–23.
- Moore RJ, Ong SS, Tyler DJ, et al. Spiral artery blood volume in normal pregnancies and those compromised by pre-eclampsia. *NMR Biomed.* 2008;21:376–380.
- Bonel HM, Stolz B, Diedrichsen L, et al. Diffusion-weighted MR imaging of the placenta in fetuses with placental insufficiency. *Radiology* 2010;257:810–819.
- Sohlberg S, Mulic-Lutvica A, Olovsson M, et al. Magnetic resonance imaging-estimated placental perfusion in fetal growth assessment. *Ultrasound Obstetrics Gynecol.* 2015;46:700–705.
- Song F, Wu W, Qian Z, Zhang G, Cheng Y. Assessment of the placenta in intrauterine growth restriction by diffusion-weighted imaging and proton magnetic resonance spectroscopy. *Reproductive Sci.* 2017;24:575–581.
- Van Dusschoten D, Moonen CTW, Adrie De Jager P, Van As H. Unraveling diffusion constants in biological tissue by combining Carr–Purcell–Meiboom–Gill imaging and pulsed field gradient NMR. *Magn Reson Med.* 1996;36:907–913.

28. Peled S, Cory DG, Raymond SA, Kirschner DA, Jolesz FA. Water diffusion, T_2 , and compartmentation in frog sciatic nerve. *Magn Reson Med*. 1999;42:911–918.
29. Does MD, Gore JC. Compartmental study of diffusion and relaxation measured in vivo in normal and ischemic rat brain and trigeminal nerve. *Magn Reson Med*. 2000;43:837–844.
30. Hürlimann MD, Venkataramanan L. Quantitative measurement of two-dimensional distribution functions of diffusion and relaxation in grossly inhomogeneous fields. *J Magn Reson*. 2002;157:31–42.
31. Callaghan PT, Godefroy S, Ryland BN. Diffusion-relaxation correlation in simple pore structures. *J Magn Reson*. 2003;162:320–327.
32. Callaghan PT, Godefroy S, Ryland BN. Use of the second dimension in PGSE NMR studies of porous media. *Magn Reson Imaging* 2003;21:243–248.
33. Bernin D, Topgaard D. NMR diffusion and relaxation correlation methods: new insights in heterogeneous materials. *Current Opinion Colloid Interface Sci*. 2013;18:166–172.
34. De Almeida Martins JP, Topgaard D. Multidimensional correlation of nuclear relaxation rates and diffusion tensors for model-free investigations of heterogeneous anisotropic porous materials. *Sci Rep*. 2018;8:2488.
35. De Santis S, Barazany D, Jones DK, Assaf Y. Resolving relaxometry and diffusion properties within the same voxel in the presence of crossing fibres by combining inversion recovery and diffusion-weighted acquisitions. *Magn Reson Med*. 2016;75:372–380.
36. Kim D, Doyle EK, Wisnowski JL, Kim JH, Haldar JP. Diffusion-relaxation correlation spectroscopic imaging: a multidimensional approach for probing microstructure. *Magn Reson Med*. 2017;78:2236–2249.
37. Veraart J, Novikov DS, Fieremans E. TE dependent Diffusion Imaging (TEdDI) distinguishes between compartmental T_2 relaxation times. *NeuroImage* 2018;182:360–369.
38. Benjamini D, Basser PJ. Magnetic resonance microdynamic imaging reveals distinct tissue microenvironments. *NeuroImage* 2017;163:183–196.
39. Melbourne A, Aughwane R, Sokolska M, et al. Separating fetal and maternal placenta circulations using multiparametric MRI. *Magn Reson Med*. 2019;81:350–361.
40. Hutter J, Slator PJ, Christiaens DC, et al. Integrated and efficient diffusion-relaxometry using ZEBRA. *Sci Reports* 2018, <https://doi.org/10.1038/s41598-018-33463-2>.
41. Le Bihan D, Breton E, Lallemand D, Aubin MLL, Vignaud J, Laval-Jeantet M. Separation of diffusion and perfusion in intravoxel incoherent motion MR imaging. *Radiology* 1988;168:497–505.
42. Jerome NP, D'Arcy JA, Feiwei T, et al. Extended T_2 -IVIM model for correction of TE dependence of pseudo-diffusion volume fraction in clinical diffusion-weighted magnetic resonance imaging. *Phys Med Biol*. 2016;61:N667–N680.
43. Menon RS, Allen PS. Application of continuous relaxation time distributions to the fitting of data from model systems and excised tissue. *Magn Reson Med*. 1991;20:214–227.
44. Ronen I, Moeller S, Ugurbil K, Kim DS. Analysis of the distribution of diffusion coefficients in cat brain at 9.4 T using the inverse Laplace transformation. *Magn Reson Imaging* 2006;24:61–68.
45. Bai R, Koay CG, Hutchinson E, Basser PJ. A framework for accurate determination of the T_2 distribution from multiple echo magnitude MRI images. *J Magn Reson*. 2014;244:53–63.
46. Ahola S, Zhivonitko VV, Mankinen O, et al. Ultrafast multidimensional Laplace NMR for a rapid and sensitive chemical analysis. *Nat Commun*. 2015;6:1–7.
47. English AE, Whittall KP, Joy MLG, Henkelman RM. Quantitative Two-dimensional time correlation relaxometry. *Magn Reson Med*. 1991;22:425–434.
48. Tranquilli AL, Dekker G, Magee L, et al. The classification, diagnosis and management of the hypertensive disorders of pregnancy: a revised statement from the ISSHP. *Pregnancy Hypertension* 2014;4:97–104.
49. Slator PJ, Hutter J, Jackson L, Rutherford M, Hajnal J, Alexander D. Optimised B-values & gradient directions for placental diffusion MRI, ISMRM workshop on placental MRI. 2018.
50. Hutter J, Slator PJ, Jackson L, et al. Multi-modal functional MRI to explore placental function over gestation. *Magn Reson Med*. 2019;81:1191–1204.
51. Does MD. MERA Toolbox, Version 2. https://vuiis.vumc.org/doesmd/MERA/MERA_Toolbox.html.
52. Whittall KP, MacKay AL. Quantitative interpretation of NMR relaxation data. *J Magn Reson*. 1989;84:134–152.
53. Schabel MC, Roberts VHJ, Lo JO, et al. Functional imaging of the nonhuman primate placenta with endogenous blood oxygen level-dependent contrast. *Magn Reson Med*. 2016;76:1551–1562.
54. Lo JO, Roberts VHJ, Schabel MC, et al. Novel detection of placental insufficiency by magnetic resonance imaging in the nonhuman primate. *Reproductive Sci*. 2017;25:193371911769970.
55. Solomon E, Avni R, Hadas R, et al. Major mouse placental compartments revealed by diffusion-weighted MRI, contrast-enhanced MRI, and fluorescence imaging. *Proc Nat Acad Sci*. 2014;111:10353–10358.
56. Sinding M, Peters DA, Frøkjær JB, et al. Placental magnetic resonance imaging T_2^* measurements in normal pregnancies and in those complicated by fetal growth restriction. *Ultrasound Obstetrics Gynecol*. 2016;47:748–754.
57. Kim CJ, Romero R, Chaemsaithong P, Kim JS. Chronic inflammation of the placenta: definition, classification, pathogenesis, and clinical significance. *Am J Obstetrics Gynecol*. 2015;213:S53–S69.
58. Slator PJ, Hutter J, İanus A, et al. A framework for calculating time-efficient diffusion MRI protocols for anisotropic IVIM and an application in the placenta. In 2018 MICCAI Workshop on Computational Diffusion MRI (CDMRI'18); 2018.

SUPPORTING INFORMATION

Additional supporting information may be found online in the Supporting Information section at the end of the article.

TABLE S1 Overview of placental T_2^* and dMRI studies to date

FIGURE S1 Exemplary raw volumes from placental diffusivity-relaxometry scan. The resolution was 2 mm isotropic—see Experiments section in Methods for further acquisition parameters. We display 70 out of the full set of 330 contrast encodings. Note that each row has a different color scaling. Figure 3 shows the derived T_2^* -ADC spectrum and maps for this scan

FIGURE S2 T_2^* -ADC spectra derived from inverse Laplace transforms of the spatially averaged signal within placenta ROIs. Horizontal dashed blue lines represent the approximate diffusivity of water in free media at 37°C ($3 \times 10^{-3} \text{ mm}^2 \text{ s}^{-1}$)

FIGURE S3 Spectral volume fraction maps, obtained by summing the T_2^* -ADC spectrum weight within the domain where $ADC < 25 \times 10^{-3} \text{ mm}^2 \text{ s}^{-1}$

FIGURE S4 As Figure S3, but for the domain where $25 \times 10^{-3} \text{ mm}^2 \text{ s}^{-1} < ADC < 200 \times 10^{-3} \text{ mm}^2 \text{ s}^{-1}$

FIGURE S5 As Figure S3, but for the domain where $200 \times 10^{-3} \text{ mm}^2 \text{ s}^{-1} < ADC < 1000 \times 10^{-3} \text{ mm}^2 \text{ s}^{-1}$

FIGURE S6 Correlation between T_2^* and ADC from combined ADC- T_2^* fit within placental ROIs. Horizontal blue dashed lines represents the approximate diffusivity of water in free media at 37°C ($3 \times 10^{-3} \text{ mm}^2 \text{ s}^{-1}$)

How to cite this article: Slator PJ, Hutter J, Palombo M. Combined diffusion-relaxometry MRI to identify dysfunction in the human placenta. *Magn Reson Med.* 2019;82:95–106. <https://doi.org/10.1002/mrm.27733>